

γ -Valerolactone: A Nontoxic Green Solvent for Highly Stable Printed Mesoporous Perovskite Solar Cells

Carys Worsley, Dimitrios Raptis, Simone Meroni, Alexander Doolin, Rodrigo Garcia-Rodriguez, Matthew Davies, and Trystan Watson*

Mesoscopic carbon-based lead halide perovskite solar cells (CPSCs) represent a promising architecture for commercialization in the field of perovskite photovoltaics as they are stable, potentially low cost, and use easily scaled production methods. However, the use of toxic and psychoactive solvents such as dimethylformamide (DMF) and γ -butyrolactone (GBL) currently limits their commercial viability: DMF introduces a significant health risk and GBL is subject to legal restrictions in many countries. The development of safe and effective solvent systems is therefore an essential step toward commercial viability. Herein, γ -valerolactone (GVL) is presented as a nontoxic, biodegradable, green alternative to GBL for CPSC fabrication. Cells fabricated with a precursor concentration of 1.1 M and annealed at 45 °C exhibit comparable performance to standard GBL devices, achieving a champion power conversion efficiency (PCE) of 12.91% in a device of 1 cm² active area. Herein, it is proven that GVL is a viable alternative to GBL for CPSCs and enables research in countries where GBL is legally restricted and makes large-scale CPSC manufacture more sustainable.

limited by poor device stability under operating conditions; perovskites are particularly sensitive to humidity as well as exhibiting UV, thermal, and oxygen sensitivity in many architectures.^[9–12] In addition, many device architectures use prohibitively expensive or toxic components or manufacturing methods inherently unsuitable for large-scale production. Expensive and unstable organic hole extraction materials (HTMs) such as spiro-OMeTAD are particularly problematic. This has led to significant research on alternative materials such as NiO and work on hole conductor free carbon-based devices with improved operational stability.^[13–16]

Mesoscopic carbon-based perovskite solar cells (CPSCs) make use of easily scaled manufacturing processes and are frequently described as one of the frontrunners for perovskite commercialization.

Fabricated via sequential screen printing of mesoporous TiO₂, ZrO₂, and carbon before drop casting of the perovskite precursor, CPSCs are highly stable, benefitting from both the lack of a hole transporter and the presence of a >20 μ m-thick, encompassing mesoporous scaffold, which provides mechanical stability and limits oxygen and moisture access.^[17] Performance and stability are further enhanced by incorporating 5-aminovaleric acid (AVAI) to improve precursor infiltration, induce highly stable 2D/3D crystal formations at the perovskite–TiO₂ interface, and limit superoxide production.^[17,18] Polyurethane/glass-encapsulated devices produced using AVA_(x)MA_(1-x)PbI₃ γ -butyrolactone (GBL) perovskite precursors recently passed stringent IEC61215:2016 tests, including damp heat tests (85 °C at 85% relative humidity (RH), for 1100 h), thermal cycling tests (–40 to 85 °C for 200 cycles), UV preconditioning tests (60 °C, 50 kWh m⁻²), and maximum power point testing light-soaking tests (55 °C, 9000 h).^[19]


This impressive stability combined with the use of scalable deposition techniques make CPSCs attractive for commercial development, and manufacturing bottlenecks are already being addressed in the scientific literature, for example, using near-infrared annealing and robotic infiltration methods to drastically reduce heating times and automate infiltration.^[18,20,21] However, significant barriers to commercial application still exist.^[22,23] For example, the most common precursor solvents for CPSCs, dimethylformamide (DMF)–dimethyl sulfoxide (DMSO) mixtures

1. Introduction

Since their advent in 2009, lead halide perovskite solar cells (PSCs) have rapidly progressed to exhibit power conversion efficiencies (PCEs) of 25.5%, approaching that of commercially available monocrystalline silicon devices.^[1–4] In addition to exhibiting excellent carrier mobility, high absorption coefficients, tunable bandgaps, and unusual defect tolerance, these semiconductors are cheap and amenable to low-cost solution-based processing.^[5–8]

To be considered commercially viable, stable, high-efficiency devices must be easily and reproducibly attainable at large scale for low-cost per watt peak. PSC commercialization is currently

C. Worsley, Dr. D. Raptis, Dr. S. Meroni, A. Doolin, Dr. R. Garcia-Rodriguez, Dr. M. Davies, Prof. T. Watson
SPECIFIC IKC, College of Engineering
Swansea University Bay Campus
Fabian Way, Crymlyn Burrows, Skewen, Swansea SA1 8EN, UK
E-mail: t.m.watson@swansea.ac.uk

 The ORCID identification number(s) for the author(s) of this article can be found under <https://doi.org/10.1002/ente.202100312>.

© 2021 The Authors. Energy Technology published by Wiley-VCH GmbH. This is an open access article under the terms of the Creative Commons Attribution License, which permits use, distribution and reproduction in any medium, provided the original work is properly cited.

DOI: 10.1002/ente.202100312

and γ -butyrolactone (GBL) systems, respectively, introduce toxicity and legality issues.^[18,19,24–27]

Toxic mixtures of DMF and DMSO present significant health and environmental hazards, particularly in the presence of solubilized lead.^[28,29] The 30 mgm^{-1} short-term exposure limit (STEL) of these mixtures coupled with a flash point within the perovskite processing window mean that large-scale production would require expensive vapor handling and solvent recovery systems.^[29] Long-term reliance on DMF as a solvent for large-scale manufacture is also potentially unviable: European Registration, Evaluation, Authorisation and Restriction of Chemicals (REACH) regulations classify DMF as a “substance of very high concern” a precursor to introducing use restrictions.^[30]

In addition, thermogravimetric analyses have shown that residual DMF is retained in perovskite films postannealing, which has unknown impact on device lifetimes and can complicate end-of-life disposal or recycling procedures. This is especially relevant to CPSCs, as the mesoporous scaffold can impede solvent removal and devices contain larger amounts of perovskite.^[31]

Although much less toxic than DMF/DMSO systems, GBL is a legally restricted psychoactive.^[32] Despite relatively low oral toxicity, the doses for psychoactive effects can be close to lethal amounts, introducing a significant health risk for users.^[33,34] As such, GBL is subject to legal restrictions in many countries. This introduces legislative costs at large scale and can hamper lab-scale research, where access to solvents is prohibited.

It is clear that a greener, nonhazardous solvent would improve the commercial viability of CPSCs. Fully biodegradable, readily available from sustainable lignocellulosic biomass feedstocks, and frequently used as a food and perfume additive, GVL is over five times less toxic than GBL (GVL LD_{50} oral-rat = 8800 mg kg^{-1} , GBL LD_{50} oral-rat = $1540 - 1800 \text{ mg kg}^{-1}$).^[35–37] GVL has been used as an additive in conjunction with DMF in conventional sandwich PSCs but to our knowledge is yet to be applied in printable mesoscopic CPSCs or as the sole precursor solvent in a photovoltaic (PV) device.^[38] In this work, GVL is presented as a nontoxic GBL alternative for fabricating highly stable CPSCs. Furthermore, the legal restrictions that impact GBL availability in certain countries do not apply to GVL, making it more suited to large-scale sustainable production. This work can therefore provide an avenue toward more commercially viable CPSCs and enable continued CPSC research in countries where GBL is prohibited.

2. Results and Discussion

In CPSCs, the perovskite precursor is generally incorporated into the mesoscopic triple stack via drop casting through the top electrode. Significant precursor penetration of the base TiO_2 layer can even be observed during the first-minute, followed by drop casting of GBL precursors, although 10 min percolation time is generally allowed (Figure 1).^[17–19,39] Conventional $\text{AVA}_{0.03}\text{MAPbI}_3$ -GBL devices are generally annealed for 1 h at 50°C in ambient conditions.^[17–19,23]

Solvent systems heavily impact the colloidal nature of precursors, the quality of infiltration, and the crystallinity of annealed perovskite. Precursors utilizing different solvents can require different annealing conditions for quality MAPbI_3 formation and stack infiltration. Therefore, UV–vis analysis of precursor solutions and X-ray diffraction (XRD) of infiltrated TiO_2 scaffolds was conducted before initial device trials to compare the precursor absorption characteristics and confirm that the GVL-based solutions formed MAPbI_3 without degradation under standard GBL annealing conditions.

As a more viscous solvent of slightly different chemical structure, the colloidal composition of GVL precursors may be different to that of GBL.^[40–42] Solvents of lower Gutman donor numbers (D_n) coordinate less easily to Pb^{2+} centers, leading to increased Pb–I interactions, larger colloidal networks, and correspondingly larger crystal sizes.^[40,41] As shown in the surface scanning electron microscope (SEM) images (Figure S1, Supporting Information), the annealed GVL sample presented smaller surface crystals than those crystallized from GBL, which produced larger crystals and areas of lower-quality crystals (Figure S1, Supporting Information). This suggests that GVL coordinates more readily to Pb^{2+} centers and may form smaller colloids.

The coordination of solvents to Pb^{2+} centers can be probed by comparing the UV–vis absorption of diluted precursors. When solvent– Pb^{2+} coordination is less favorable, greater proportions of I^- interact with the metal ions and the relative concentration of highly coordinated iodoplumbates increases.^[40,42,43] In a dilute precursor this changes the relative absorption intensities of solvated PbI_2 , PbI_3^- , and PbI_4^{2-} , which have been shown to indicate changes in colloidal diameters.^[40,42,43]

As shown in Figure 2, UV–vis spectra of GVL precursors diluted to 175 mmol showed a higher relative PbI_2 absorbance peak at $\approx 320 \text{ nm}$, whereas the $[\text{PbI}_3]^-$ peak at $\approx 380 \text{ nm}$ was much more pronounced in the GBL solutions.^[40] This suggests that the GVL coordinates more readily to the Pb^{2+} centers than GBL and can explain the slightly larger GBL crystal sizes and

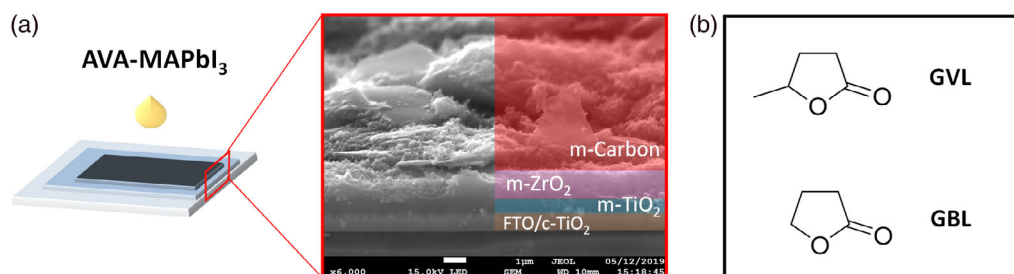


Figure 1. a) Schematic representation of CPSC infiltration procedure with the corresponding cross-sectional SEM of an uninfiltrated stack and labeled layers. b) Chemical structures of GVL and GBL.

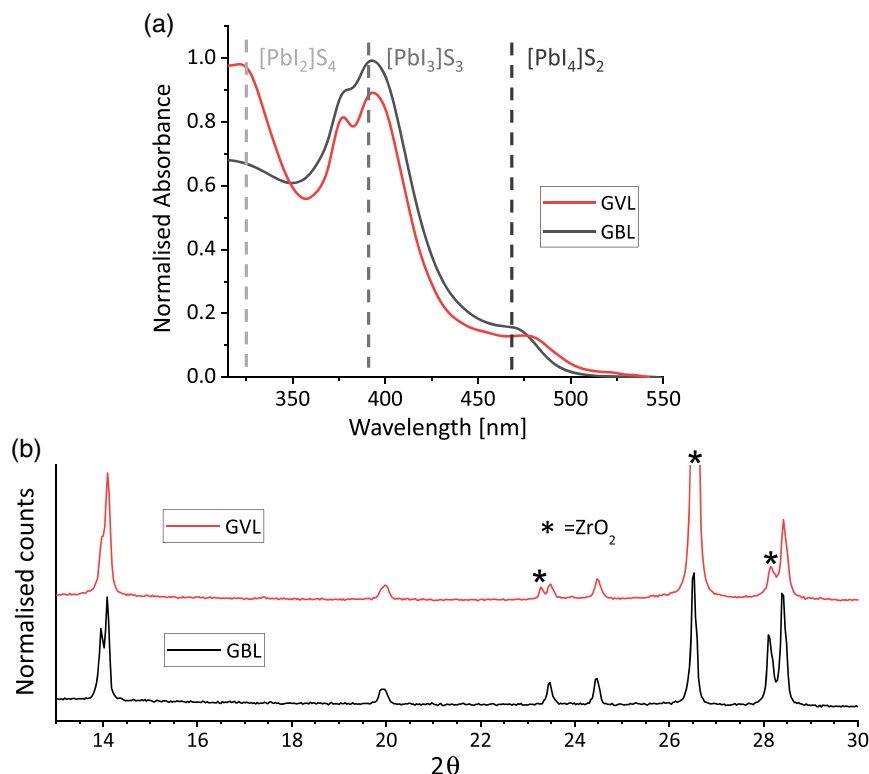


Figure 2. a) UV–vis spectra of 175 mmol AVA_{0.03}MAPbI₃ precursors in GVL and GBL. b) XRD patterns of AVA_{0.03}MAPbI₃ perovskites on mesoporous ZrO₂/FTO/glass, annealed from GVL (red) and GBL (black) precursors.

superior stability of GVL precursors toward precipitation (Figure S2, Supporting Information).^[43]

Finally, to compare the perovskite crystallinity, phase formation, and ensure that no degradation to PbI₂ occurs during standard annealing conditions, XRD was conducted.

As shown in Figure 2c, both samples showed identical peak positions. This indicates that the MAPbI₃ unit cells are the same size and that the phase composition of both samples is similar. In addition, the lack of a PbI₂ peak at $2\theta \approx 12.5^\circ$ suggests that complete conversion to MAPbI₃ with no subsequent degradation occurred with the standard GBL annealing procedure.

Interestingly, the relative intensity of the $2\theta = 14.13^\circ$ peak is higher in the GVL samples (Figure 2b). This can be indicative of improved crystallinity and is typical of preferential growth in the (110) direction and can account for the more defined shapes of surface crystals observed for GVL (Figure S1, Supporting Information).^[19] As both samples exhibited similar crystal phase formation and no significant degradation, the 50 °C GBL annealing procedure was deemed suitable for initial GVL-based device trials.

The AVA_{0.03}MAPbI₃-GVL cells annealed at 50 °C exhibited an average PCE of 9.9%, only slightly lower than the average GBL PCE of 10.3% (Figure 3). Although GVL devices exhibited slightly lower J_{sc} and FF values, this was counteracted by consistently higher V_{oc} . Decreased J_{sc} accompanied by V_{oc} increases can be indicative of an increased perovskite bandgap, although this is unlikely here, given that the same perovskite formulation is present in both samples. The increased V_{oc} values are therefore

more likely a consequence of higher crystallinity (Figure 2): higher quality perovskite crystals have fewer shallow traps near the band edge, so less nonradiative recombination occurs under illumination.^[44] In this case, the lower J_{sc} and FF values are likely instead due to poor perovskite infiltration, as insufficient perovskite contact with charge extraction layers impedes carrier collection. Photoluminescence (PL), external quantum efficiency (EQE), and PL quantum yield analyses were therefore conducted to compare the absorption spectra, optical bandgaps, emissivity, and levels of recombination in GVL and GBL-based samples.

As shown in Figure 4, the PL emission intensity of GVL perovskites in ZrO₂ scaffolds was far higher than that of the GBL samples.^[44] In addition, the calculated photoluminescence quantum yield (PLQY) values of GVL samples were also superior, at 0.19% and 0.06% for GVL and GBL samples, respectively. This indicates that there are lower levels of nonradiative recombination in the GVL-annealed AVA_{0.03}MAPbI₃ and offers further proof that GVL-annealed AVA_{0.03}MAPbI₃ is of higher quality than that crystallized from GBL precursors.^[44]

A slight blue-shift in the emission peak of the GVL samples can be observed, with samples experiencing some photodarkening during the initial measurements (Figure S3, Supporting Information). This can be caused by several factors, including decreased grain sizes, shifts in the band edge, or sample degradation.^[45,46] Sample degradation is often accompanied by blue-shifting of the emission peak over time and increased levels of nonradiative recombination, as shown in the study by Pean et al.^[46] In this case, the emission peak position did not

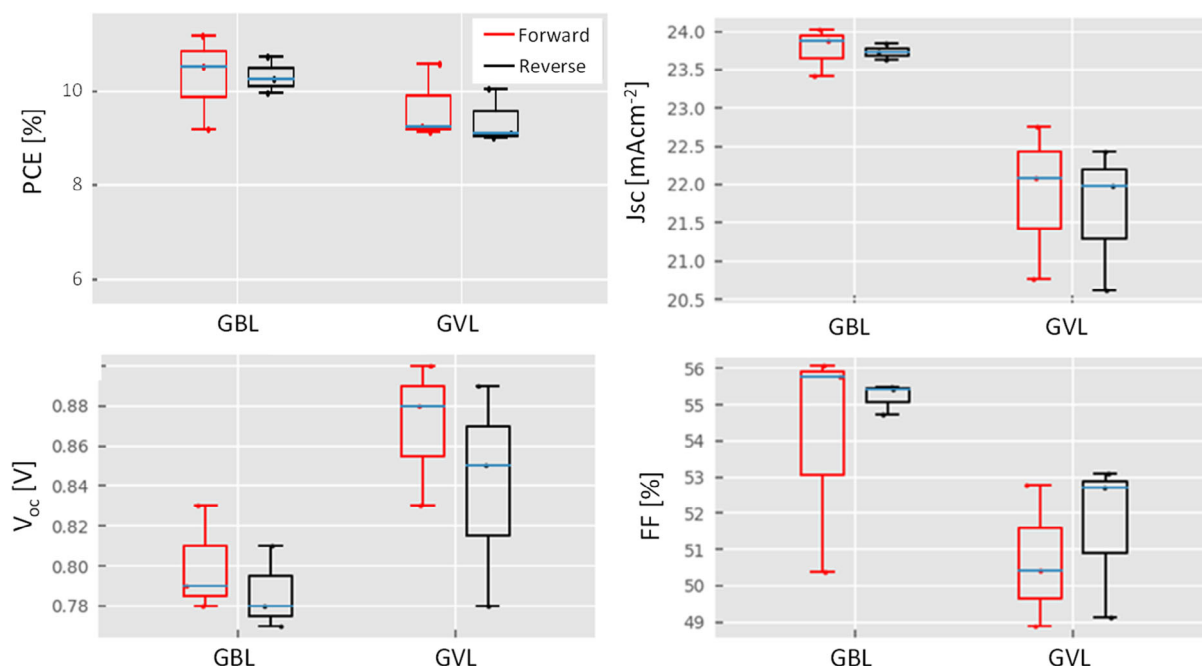


Figure 3. Photovoltaic parameters for initial devices fabricated from 0.95 M GBL and GVL-based $\text{AVA}_{0.03}\text{MAPbI}_3$ precursors and annealed at 50 °C. Three samples for each set.

change over multiple measurements and the photodarkening behavior stabilized within ten measurements. The slightly lower performance of GVL devices annealed at 50 °C is therefore unlikely to be a consequence of changes in the material bandgap or instability, and the observed PL blue-shift is likely a consequence of smaller crystals (Figure S1, Supporting Information).^[44]

This is further supported by the EQE measurements, where the calculated material bandgaps were comparable between both sets, with GVL samples showing improved absorption intensity in the 600–800 nm range (Figure 4). Longer wavelengths are absorbed deeper in the stack, and such improved absorption can suggest that the GVL samples have a higher proportion of perovskite in the ZrO_2 layer than in the TiO_2 .^[47] This is indicative of comparatively poor TiO_2 filling in the GVL devices.

Although the GVL EQE intensities are also less consistent than those of the GBL samples, it should be noted that EQE intensities are often highly variable in CPSCs as inconsistencies in perovskite infiltration can lead to changes in absorption efficiency across the active area. Mismatches between the $I-V$ J_{sc} and EQE photocurrent are also common as $I-V$ curves are obtained after long light-soaking periods.^[48] EQE photocurrents are therefore not representative of device performance or photocurrents after light soaking, and variations in EQE intensity between sample sets should not be used to compare infiltration.^[18] However, when observed in conjunction with increased absorption of higher-wavelength light and supporting $I-V$ evidence of lower J_{sc} and FF values, highly variable EQE intensities can be an indication of poor perovskite infiltration.

This can be a consequence of detrimentally fast perovskite crystallization: If nucleation occurs too fast, growing crystals can form blockages that prevent full infiltration, leading to voids

in the annealed stack. Such devices typically present as uneven or gray in color due to poor TiO_2 filling. Recent work has shown that CPSC infiltration may be improved through vapor-assisted crystallization, where devices are kept in a closed solvent vapor environment during some or all of the annealing process (Figure S4, Supporting Information). This solvent evaporation-controlled (SEC) crystallization allows more time for precursor percolation and reduces the rate of crystal growth to form larger, more densely packed crystals.^[27,49]

A 1 h SEC treatment at 50 °C was therefore applied to devices infiltrated with GVL and GBL-based $\text{AVA}_{0.03}\text{MAPbI}_3$ precursors before standard annealing at 50 °C. SEC-treated GBL-based devices were more reproducible and generally exhibited lower hysteresis. However, SEC treatment of GVL devices resulted in visibly poor infiltration and low J_{sc} and FF (Figure S4, Supporting Information). It was hypothesized that for the GVL system, solvent loss from the stack during the SEC treatment resulted in a highly saturated, poorly wetting solution within the scaffold, which then annealed extremely fast on removal of the Petri dish.

This suggests that GVL systems are more sensitive to detrimentally fast crystal growth. It was postulated that a lower annealing temperature could mitigate this problem by slowing the rate of solvent removal without the need for additives or additional annealing steps. Devices were therefore fabricated with a range of annealing temperatures (40, 45, 50, and 60 °C).

As shown in **Figure 5**, an annealing temperature of 45 °C produced the best devices, with the champion device exhibiting of 21.6 mA cm^{-2} J_{sc} , 916 mV V_{oc} , 58% FF, and 11.4% PCE (average 11.13% \pm 0.31% PCE, 919 \pm 4 mV V_{oc} , 56.6% FF, 21.38 \pm 0.34 mA cm^{-2} J_{sc}). This is reflected in the stabilized current measurements, where devices annealed at 45 °C far outperformed those prepared at other temperatures (average

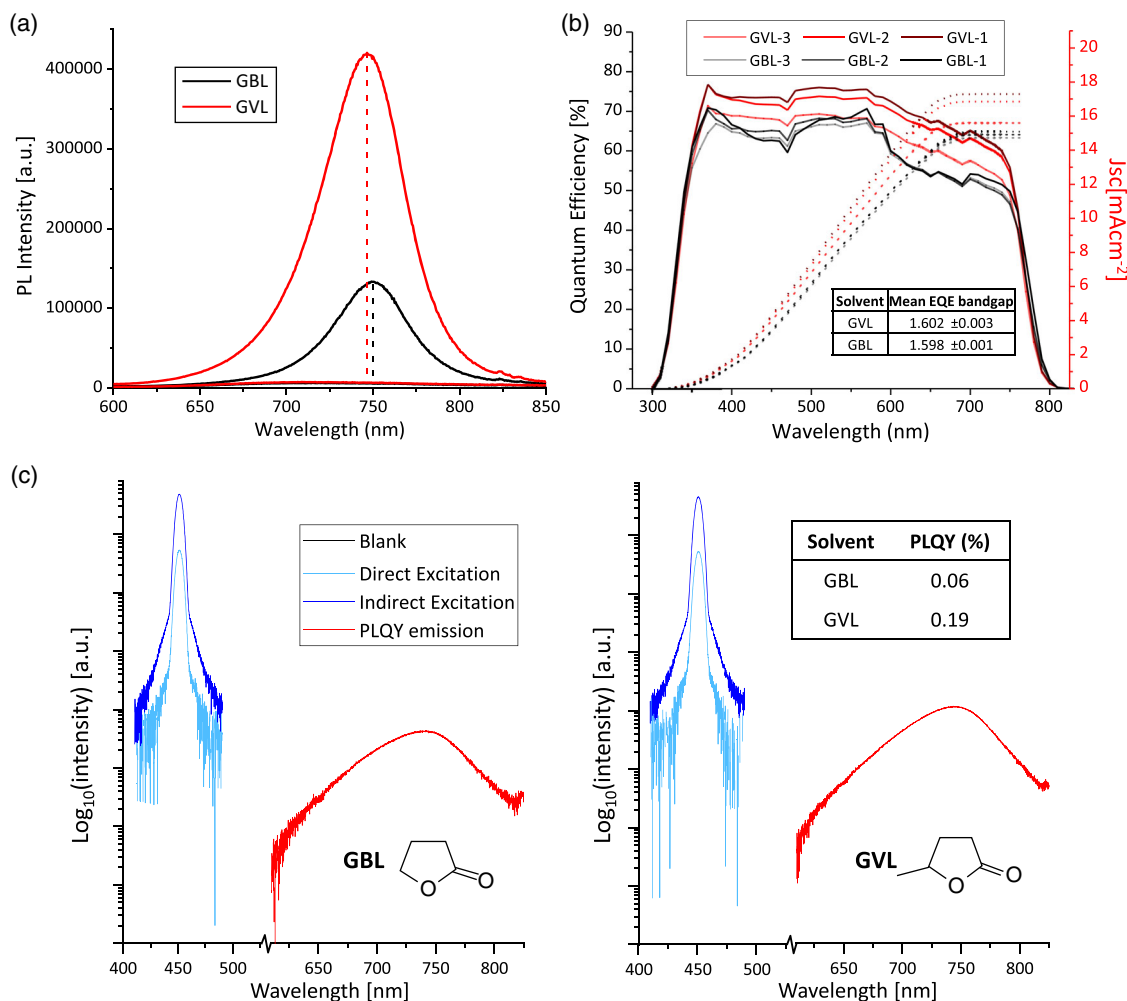


Figure 4. a) Steady-state PL emission of MAPbI₃ perovskites crystallized from 0.95 M AVA_{0.03}MAPbI₃ in GVL and GBL in ZrO₂/carbon scaffolds on glass. b) EQE results from 300–800 nm for three GBL (GBL-1, -2, and -3) and three GVL devices (GVL-1, -2, and -3) with an inlaid table showing average calculated EQE bandgaps. c) PLQY data for ZrO₂/carbon scaffolds on glass infiltrated with GBL (right) and GVL (left) AVA_{0.03}MAPbI₃ precursor. Graphs show all excitation data and the corresponding corrected emission of each sample. Calculated external PLQY values are shown in the inlaid table.

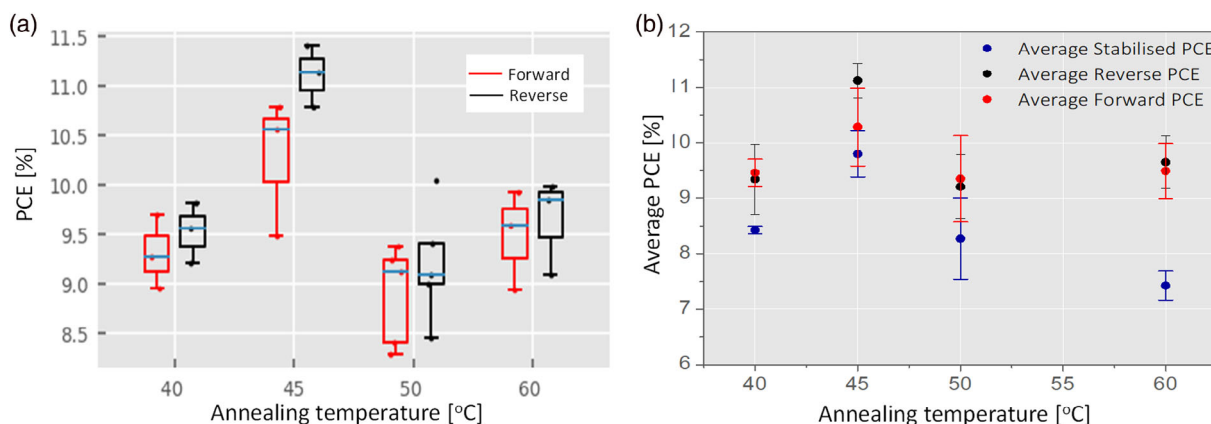


Figure 5. Left: Box plots of average PCEs from *I*–*V* curves for GVL devices annealed at different temperatures. Right: Average forward (red), reverse (black), and stabilized (blue) PCEs. Four samples for each set.

stabilized PCE: $9.80\% \pm 0.42\%$ (Figure 5), champion stabilized result of 10.2%). Box plots showing the full $I-V$ parameters and representative $I-V$ curves for devices made at different temperatures are shown in Figure S6, Supporting Information.

Such discrepancy between stabilized and $I-V$ PCEs is common in CPSCs, where $I-V$ calculations frequently overestimate performance due to imbalanced charge extraction at device electrodes.^[50] Although these problems can be somewhat mitigated by long light-soaking procedures and slow scan rates, $I-V$ PCEs are still frequently higher than those from stabilized current measurements. Poor infiltration decreases the perovskite–electrode contact, further hindering charge extraction and exacerbating PCE overestimation from $I-V$ curves.^[50] In other words, poorly infiltrated samples tend to exhibit larger differences between PCEs calculated from $I-V$ curves and those from stabilized current measurements.^[50]

This is clearly the case in the 60 °C samples, where there are many perovskite-free voids visible in the TiO₂ layer (Figure 6), and there is a marked discrepancy between the $I-V$ ($9.65\% \pm 0.47\%$) and stabilized ($7.42\% \pm 0.26\%$) PCEs (Figure 5). Conversely, the optimum 45 °C sample shows particularly dense ZrO₂ infiltration with larger, more continuous perovskite crystals (Figure 6) and much more comparable $I-V$ and stabilized PCE values.

However, despite improving the device infiltration, even the optimized 45 °C device exhibited larger perovskite-free voids than the standard GBL device (Figure 6).

Precursor concentration is also known to impact infiltration. Concentrated precursors can experience detrimental nucleation during the initial infiltration stages and prevent complete precursor penetration, whereas the volume contraction experienced by dilute solutions during solvent evaporation can result in poor pore filling. The optimal concentration of the given precursor is highly dependent on solvent properties such as polarity and coordination.^[43] As dilute GVL precursors exhibited lower PbI₃⁻ absorption in the UV–vis analysis, it was hypothesized that more favorable solvent–Pb²⁺ interactions could be resulting in smaller colloidal networks and thus less continuous crystal formation. GVL precursors may therefore require higher concentrations for optimal performance. Devices were therefore fabricated with 0.7, 0.95, 1.1, and 1.25 M AVA_{0.03}MAPbI₃ GVL

precursors at the optimized 45 °C annealing temperature (Figure S6, Supporting Information).

The highest quality infiltration was achieved with a 1.10 M concentration, where dense perovskite formation was observed throughout the ZrO₂ and TiO₂ across the entire active area (Figure 7). Device performance was correspondingly higher in these devices due to superior V_{oc} . Full $I-V$ parameters for initial optimization and a following champion set can be found in Figure S5, Supporting Information and Figure 7, respectively.

The photovoltaic parameters for a batch of GVL devices fabricated with the optimized precursor (1.1 M) and annealing conditions (45 °C) are shown in Figure 8 alongside standard GBL devices. The GVL devices exhibited an average PCE of $12.44\% \pm 0.56\%$ (champion PCE: 12.91%, 11.3% stabilized, Figure S7, Supporting Information), higher than that of the GBL control devices at $11.67\% \pm 0.40\%$ (Figure 7). The $I-V$ curves of the champion device are shown in Figure S7, Supporting Information. All the $I-V$ parameters are higher on average in the GVL devices, with notably high and reproducible V_{oc} (0.90 ± 0.013 V and 0.82 ± 0.017 V for GVL and GBL, respectively). There was also reduced hysteresis in the GVL devices, although it should be noted that this is not the case for every batch: the hysteresis of GVL and GBL batches were generally comparable across other batches (Figure 3, 7 and Figure S6, Supporting Information).

One of the major advantages of GBL-based AVA_{0.03}MAPbI₃ mCPSCs is their inherent stability. Any potential GBL replacement must therefore produce devices of similar stability to be considered a viable alternative. Notably, even the concentrated GVL precursors were much more stable to precipitation at room temperature (Figure 8): Standard 0.95 M AVA_{0.03}MAPbI₃ in GBL forms precipitates when stored at room temperature, whereas all the fabricated GVL precursors were stable. This would be advantageous in a commercial setting, removing the need for redissolution prior to manufacture and decreasing the risk of equipment blockages.

Encapsulated devices were therefore subjected to long-term light exposure at 0.85 sun, elevated temperature (≈ 40 °C), and ambient humidity (40–70%). As shown in Figure 8, minimal performance loss was observed in both devices over 550 h of continuous illumination: the GVL device performance fell 7.8%,

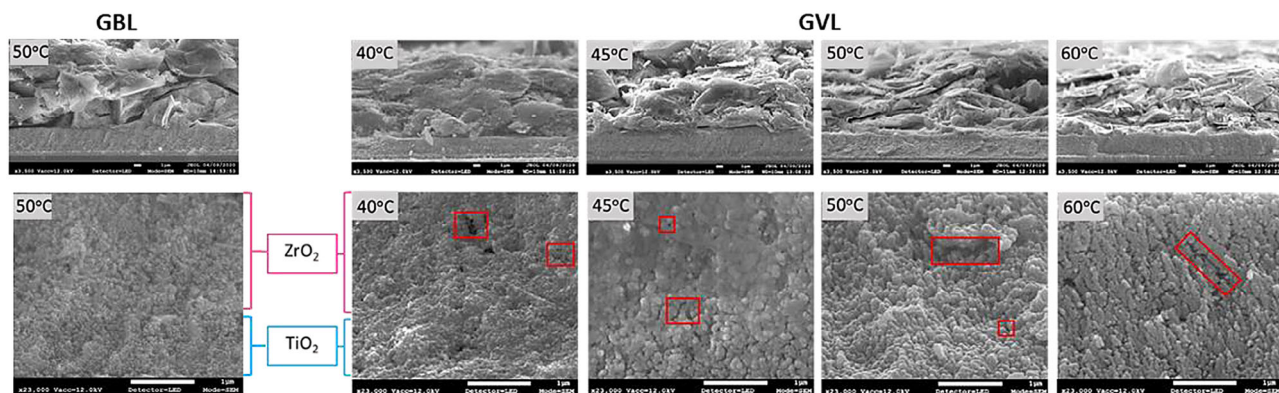


Figure 6. Cross-sectional SEM images of CPSCs infiltrated with 0.95 M AVA_{0.03}MAPbI₃ in GBL (left) and GVL (right) and annealed at different temperatures. Above: all three layers at 3500× magnification. Below: TiO₂/ZrO₂ layers at 23 000× magnification. Dark patches or gaps in the layer represent perovskite-sparse voids. Examples of different size voids are highlighted with red boxes.

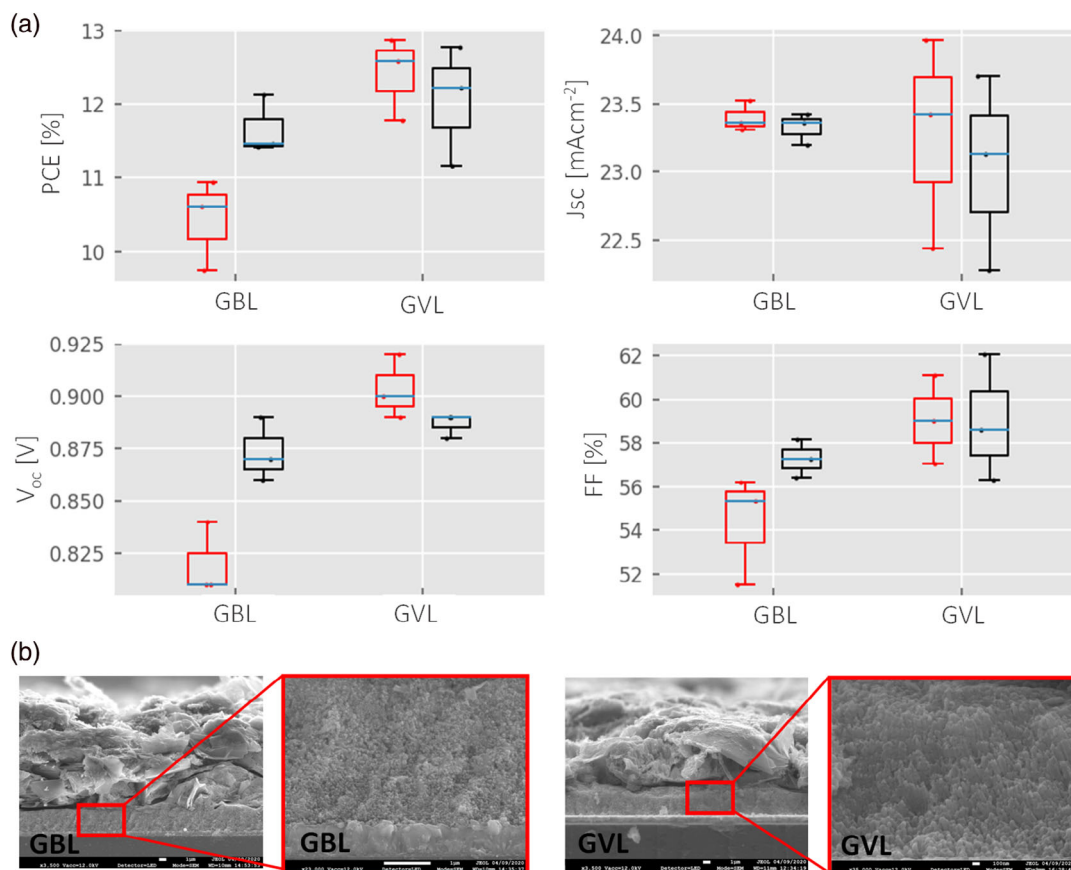


Figure 7. a) Box plots showing photovoltaic parameters of GBL devices compared with the optimized GVL system. b) Cross-sectional SEM images of devices made using standard GBL (0.95 M) and optimized GVL (1.1 M) precursors. Three devices in each set.

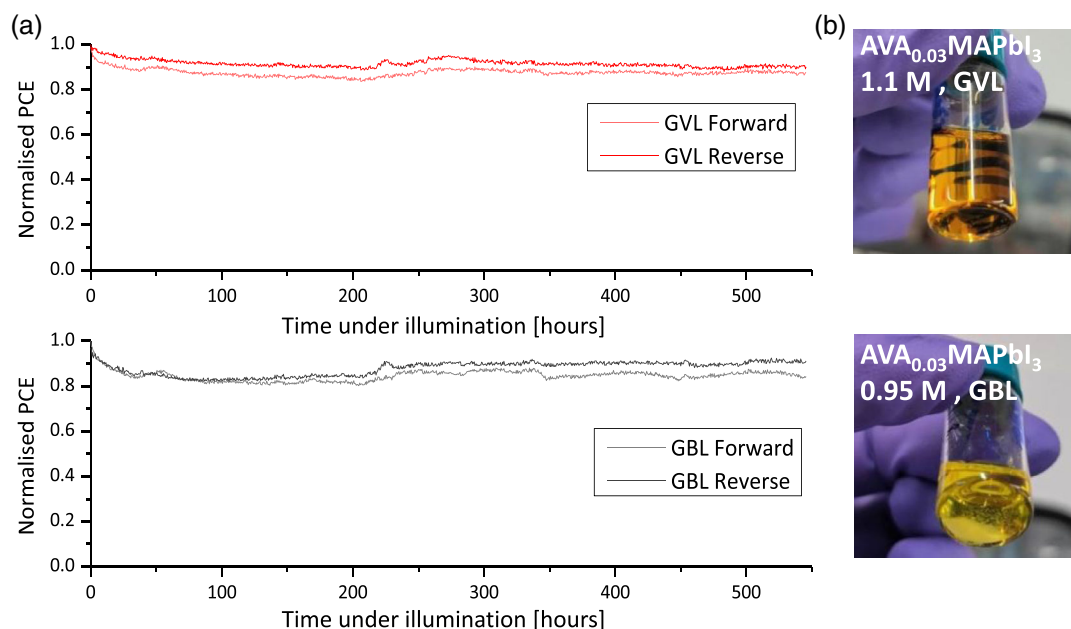


Figure 8. Left: Images of optimized 1.1 M GVL (above) and 0.95 GBL (below) precursors after 1 week of storage at room temperature. Normalized PCEs of GVL (above) and GBL (below) devices over time. Devices were kept under an illumination of 0.85 sun at $\approx 40^\circ\text{C}$ and ambient humidity (50–70%) and measured every 30 min for the duration.

whereas the GBL device fell 8.9%. The comparable stability of the two samples proves that GVL is a viable replacement for GBL in the fabrication of highly stable AVA_{0.03}MAPbI₃ devices.

3. Conclusion

Printable AVA-MAPbI₃ CPSCs are frequently cited as the most commercially viable perovskite architecture. However, the DMF or GBL-based solvent systems used in these devices represent a significant barrier to scale up and commercial viability: DMF is highly toxic and GBL a psychoactive that is restricted in many countries.

This work presents GVL as a sustainable, nontoxic novel solvent for CPSC fabrication. Five times less toxic than GBL, GVL is completely biodegradable, can be sourced from renewable lignocellulosic biomass feedstocks, and presents none of the legality issues associated with GBL. A low optimized annealing temperature of 45 °C and optimized precursor concentration of 1.1 M are shown to improve GVL precursor infiltration and produce devices of comparable efficiency with optimized GBL precursors, achieving a champion PCE of 12.91% in a 1 cm² device (11.33% stabilized). Devices exhibited superior V_{oc} to GBL controls and were stable for over 500 h of illumination with continuous testing at 40 °C and 40–60% RH. This work could therefore improve the commercial viability of CPSCs and will allow continued CPSC research in countries where GBL is prohibited.

4. Experimental Section

Materials: PbI₂ (99%, Sigma-Aldrich), MAI (CH₃NH₃I, anhydrous, Dyesol), 5-ammonium valeric acid iodide (5-AVAI, Dyesol), γ -butyrolactone (GBL, Sigma Aldrich), and γ -valerolactone (GVL, Sigma Aldrich) were used as received.

For device stacks, titanium diisopropoxide bis (acetylacetonate) (TAA, 75% in IPA, Sigma-Aldrich), anhydrous 2-propanol (IPA, 99.5%, Sigma Aldrich), TiO₂ paste (30NR-D, GreatCell Solar), ZrO₂ paste (GreatCell Solar), carbon paste (Gwent electronic materials), and terpineol (95%, Sigma-Aldrich) were used as received.

Device Fabrication: FTO substrates were patterned with a Nb:YVO₄ laser (532 nm) before cleaning with Hellmanex (\approx 2% in deionized water), rinsing with acetone and IPA, and drying with N₂. Substrates were then placed in a Nano plasma system (Diener Electronics) and plasma cleaned for 5 min in an O₂ environment. The substrate was heated to 300 °C on a hot plate and a compact TiO₂ blocking layer was deposited by spray pyrolysis of titanium di-isopropoxide-bis(acetylacetonate) (0.2 M) in IPA.

To form the mesoporous TiO₂ layer, the titania paste 30NRD was diluted 1:1 by weight in terpineol, screen printed, and sintered at 550 °C for 30 min after a slow ramp. Next, ZrO₂ and carbon were printed and annealed at 400 °C for 30 min each. All layers were printed and annealed in ambient conditions. Layer thicknesses were 600–800 nm, \approx 2.6, and \approx 17 μ m for TiO₂, ZrO₂, and carbon, respectively.

After carbon annealing, devices were cooled before drop casting of the room-temperature precursor (20 μ L, 0.95 M) MAPbI₃ with 3% molar excess 5-AVAI in GBL or GVL as stated. Devices were left for 15 min in ambient conditions after drop casting to ensure adequate infiltration, before annealing on a hot plate for 1.5 h at 40, 45, 50, or 60 °C as specified.

SECC-treated devices were covered with a Petri dish and kept at 50 °C for 1 h, after which Petri dishes were removed and annealing conducted as normal. All steps were conducted in ambient conditions excluding precursor preparation, which was conducted in N₂ glove box.

Solder contacts were applied using an ultrasonic soldering iron at 190 °C. Devices were stored in dark ambient conditions, with RH of

45–60% and temperature of 17–21 °C. Testing was conducted 3–4 days after device completion in all cases.

Device Testing: Devices were masked to 0.49 cm² and placed under a fan for testing. A Keithley 2400 source meter and class AAA solar simulator (Newport Oriol Sol3A) at 1 sun were used for J–V measurements (calibrated against a KG5 filtered silicon reference cell, Newport Oriol 91150-KG5). Devices were scanned at a rate of 0.126 Vs⁻¹ from V_{oc} to J_{sc} and vice versa after a light-soaking period of 180 s. For stabilized current measurements, devices were held at the maximum power point (as determined by the preceding I–V scan) for a period of 150–200 s to account for slow device response times.

Stability tests were conducted using a Solaronix Solixon A-20 a.m. 1.5G AAA solar simulator. Devices were kept under continuous 0.85 AM irradiation at 38–43 °C and 40–50% relative humidity. I–V curves were measured at a rate of 0.126 Vs⁻¹ from V_{oc} to J_{sc} and vice versa every 30 min for the duration.

UV–Vis: UV–vis samples were prepared by diluting precursors to 250 mmol with GVL/MeOH in the appropriate solvent ratio (0%, 5%, 10%, or 15% methanol in GVL as specified).

The diluted solution was well mixed and placed in a clean quartz cuvette of 1 cm path length for measurement. Samples were measured from 300 to 500 nm at a rate of 90 nm min⁻¹ on a Perkin Elmer Lambda 9 UV/VIS/NIR spectrophotometer.

EQE: EQE measurements were obtained using a QE X10 system (PV Measurements) from 300 and 850 nm in the direct current mode with a light spot of less than 10 mm². Wavelengths were stepped up in increments of ten, and three readings were obtained for each wavelength. A 30–35 s delay was used at each filter change to allow for slow device responses.

Cross-Sectional SEM: Cross-sectional samples were prepared by snapping fully fabricated devices. Each section was then sputtered with \approx 5 nm Pt before mounting onto a conductive metal substrate with conductive carbon/silver tape. This was attached to the SEM stage using conductive carbon/silver tape and copper tape to ensure adequate contact. Images were obtained using a JSM-7800F Field Emission SEM at 15 kV using secondary electron imaging.

Surface SEM images were obtained using a HITACHI desktop SEM in the composition mode. PL samples (prepared as earlier) were sputtered with 5 nm Pt to enhance conductivity before placing on a conductive metal stage with conductive carbon/silver tape to ensure adequate contact.

XRD: Glass substrates were first cleaned with ethanol and IPA before bar casting of \approx 5 μ m TiO₂ paste (Greatcell Solar, 30-NRD) and subsequent annealing on a hot plate at 550 °C for 30 min. About 5 μ L of the relevant precursor was drop cast onto the cooled layer and left at room temperature for 10 min to maximize infiltration. Samples were annealed at 50 °C in a fan-assisted oven for 1 h. A Bruker diffractometer with Bragg–Brentano geometry and a Cu K α radiation X-ray source was used to obtain XRD data. 2 θ scans between 7° and 65° were collected using a step size of 0.03°.

PL: Glass and FTO substrates (for ZrO₂ and TiO₂ samples, respectively) were cleaned a solution Hellmanex in deionized water (2.4%) before rinsing with ethanol and IPA and plasma cleaning in an O₂ environment for 5 min. For the TiO₂ samples, a cTiO₂ blocking layer was sprayed onto the FTO as described earlier, before screen printing of \approx 600 nm mesoporous TiO₂ using 1:1 30NRD: terpineol. ZrO₂ layers of \approx 1.6 μ m were deposited similarly on glass substrates. TiO₂ and ZrO₂ samples were annealed at 550 and 400 °C, respectively, for 30 min before screen printing of \approx 20 μ m carbon paste. Samples were annealed at 400 °C for a further 30 min.

About 20 μ L of the relevant perovskite precursor was drop cast onto the mesoporous carbon. After 15 min of percolation time in ambient conditions, samples were annealed for 1 h on a hot plate at the specified temperature.

PL spectra were obtained using an Ocean Optics USB2000+ spectrometer with an excitation wavelength of 450 nm and a 490 nm long-pass filter in the emission pathway. Samples were measured at λ = 600–850 nm with a step size of 0.5 nm and dwell time of 0.2 s. The excitation and emission bandwidths were each 3 nm.

PLQY: Samples were prepared by screen printing $\approx 2\ \mu\text{m}$ ZrO_2 ($2.5 \times 1.5\ \text{cm}$ squares) onto cleaned glass substrates. Layers were then annealed at $400\ ^\circ\text{C}$ for 30 min before deposition of $\approx 15\ \mu\text{m}$ carbon and further annealing at $400\ ^\circ\text{C}$ for 30 min. Once cooled to room temperature, samples were infiltrated with $5\ \mu\text{L}$ $0.95\ \text{M}$ GBL or GVL-based $\text{AVA}_{0.03}\text{MAPbI}_3$ precursor. Samples were left at room temperature for 10 min before annealing at $50\ ^\circ\text{C}$ for 1 h on a hot plate in ambient conditions.

Samples were measured on an FS5 spectrofluorometer (Edinburgh Instruments) with an SC-30 integrating sphere module. All measurements were made through the glass side of the sample.

Five measurements were taken for each scattering (excitation) peak. Each scattering peak was obtained with a 410–490 nm range (peak at 450 nm) using a step size of 0.1 nm and dwell time of 0.2 s. The excitation and emission bandwidth was 5 nm and a neutral density filter with an optical density of 3 was used.

Emission peaks were measured from 600 to 850 nm, and no filter was used. All other measuring conditions were the same as detailed for the excitation peaks.

Supporting Information

Supporting Information is available from the Wiley Online Library or from the author.

Acknowledgements

This work was made possible by support from the UKRI Global Challenge Research Fund project SUNRISE (EP/P032591/1) and through the funding of the SPECIFIC Innovation and Knowledge Centre by the Engineering and Physical Science Research Council [EP/N020863/1], Innovate UK [920036], and the European Regional Development Fund [c80892] through the Welsh Government. This work was also made possible by support through Royal Society International Collaboration award (ICA\R1\191321) and the Newton Fund Impact Scheme (541128962). M.L.D. and R.G. are grateful for the financial support of the EPSRC (EP/S001336/1). The authors would like to thank the Advanced Imaging of Materials (AIM) Facility at Swansea University for lending their equipment and expertise in obtaining cross-sectional images for this manuscript. The corresponding author has been updated on May 19th, 2021.

Conflict of Interest

The authors declare no conflict of interest.

Data Availability Statement

The data that supports the findings of this study are available in the supplementary material of this article.

Keywords

mesoscopic perovskite solar cells, nontoxic solvents, photovoltaics, printable perovskites, sustainable production

Received: April 20, 2021

Published online:

[1] <https://www.nrel.gov/pv/assets/pdfs/pv-efficiency-chart.20181221.pdf> (accessed: December, 2020).

[2] M. M. Lee, J. Teuscher, T. Miyasaka, T. N. Murakami, H. J. Snaith, *Science* **2012**, 338, 643.

- [3] W. S. Yang, B.-W. Park, E. H. Jung, N. J. Jeon, Y. C. Kim, D. U. Lee, S. S. Shin, J. Seo, E. K. Kim, J. H. Noh, S. Il Seok, *Science* **2017**, 356, 1376.
- [4] H. J. Snaith, *Nat. Mater.* **2018**, 17, 372.
- [5] C. Wehrenfennig, G. E. Eperon, M. B. Johnston, H. J. Snaith, L. M. Herz, *Adv. Mater.* **2014**, 26, 1584.
- [6] B. Suarez, V. Gonzalez-Pedro, T. S. Ripolles, R. S. Sanchez, L. Otero, I. Mora-Sero, *J. Phys. Chem. Lett.* **2014**, 5, 1628.
- [7] W. Rehman, D. P. McMeekin, J. B. Patel, R. L. Milot, M. B. Johnston, H. J. Snaith, L. M. Herz, *Energy Environ. Sci.* **2017**, 10, 361.
- [8] H. Huang, M. I. Bodnarchuk, S. V. Kershaw, M. V. Kovalenko, A. L. Rogach, *ACS Energy Lett.* **2017**, 2, 2071.
- [9] Y. Han, S. Meyer, Y. Dkhissi, K. Weber, J. M. Pringle, U. Bach, L. Spiccia, Y. B. Cheng, *J. Mater. Chem. A* **2015**, 3, 8139.
- [10] B. Conings, J. Drijkoningen, N. Gauquelin, A. Babayigit, J. D'Haen, L. D'Olieslaeger, A. Ethirajan, J. Verbeeck, J. Manca, E. Mosconi, F. De Angelis, H.-G. Boyen, *Adv. Energy Mater.* **2015**, 5, 1500477.
- [11] J. Yang, T. L. Kelly, *Inorg. Chem.* **2017**, 56, 92.
- [12] Z. Song, S. C. Wathage, A. B. Phillips, M. J. Heben, *J. Photonics Energy* **2016**, 6, 022001.
- [13] B. Gil, A. J. Yun, Y. Lee, J. Kim, B. Lee, B. Park, *Electron. Mater. Lett.* **2019**, 15, 505.
- [14] A. Priyadarshi, A. Bashir, J. T. Gunawan, L. J. Haur, A. Bruno, Z. Akhter, N. Mathews, S. G. Mhaisalkar, *Energy Technol.* **2017**, 5, 1866.
- [15] H. Chen, S. Yang, *J. Mater. Chem. A* **2019**, 7, 15476.
- [16] L. Fagioliari, F. Bella, *Energy Environ. Sci.* **2019**, 12, 3437.
- [17] E. V. Péan, C. S. De Castro, S. Dimitrov, F. De Rossi, S. Meroni, J. Baker, T. Watson, M. L. Davies, *Adv. Funct. Mater.* **2020**, 30, 1909839.
- [18] A. Mei, X. Li, L. Liu, Z. Ku, T. Liu, Y. Rong, M. Xu, M. Hu, J. Chen, Y. Yang, M. Grätzel, H. Han, *Science* **2014**, 345, 295.
- [19] A. Mei, S. Sheng, Y. Ming, Y. Hu, Y. Rong, W. Zhang, S. Luo, G. Na, C. Tian, X. Hou, Y. Xiong, Z. Zhang, S. Liu, S. Uchida, T. Kim, Y. Yuan, L. Zhang, Y. Zhou, H. Han, *Joule* **2020**, 4, 1.
- [20] Y. Cai, L. Liang, P. Gao, *Chin. Phys. B* **2018**, 27, 018805.
- [21] M. Duan, Y. Hu, A. Mei, Y. Rong, H. Han, *Mater. Today Energy* **2018**, 7, 221.
- [22] J. Baker, K. Hooper, S. Meroni, A. Pockett, J. McGettrick, Z. Wei, R. Escalante, G. Oskam, M. Carnie, T. Watson, *J. Mater. Chem. A* **2017**, 5, 18643.
- [23] S. M. P. Meroni, Y. Mouhamad, F. De Rossi, A. Pockett, J. Baker, R. Escalante, J. Searle, M. J. Carnie, E. Jewell, G. Oskam, T. M. Watson, *Sci. Technol. Adv. Mater.* **2018**, 19, 1.
- [24] Y. Sheng, Y. Hu, A. Mei, P. Jiang, X. Hou, M. Duan, L. Hong, Y. Guan, Y. Rong, Y. Xiong, H. Han, *J. Mater. Chem. A* **2016**, 4, 16731.
- [25] H. Zhang, H. Wang, S. T. Williams, D. Xiong, W. Zhang, C.-C. Chueh, W. Chen, A. K.-Y. Jen, *Adv. Mater.* **2017**, 29, 1606608.
- [26] Y. Hu, Z. Zhang, A. Mei, Y. Jiang, X. Hou, Q. Wang, K. Du, Y. Rong, Y. Zhou, G. Xu, H. Han, *Adv. Mater.* **2018**, 30, 1705786.
- [27] X. Hou, M. Xu, C. Tong, W. Ji, Z. Fu, Z. Wan, F. Hao, Y. Ming, S. Liu, Y. Hu, H. Han, Y. Rong, Y. Yao, *J. Power Sources* **2019**, 415, 105.
- [28] MSDS – 227056, <https://www.sigmaaldrich.com/MSDS/MSDS/DisplayMSDSPage.do?country=GB&language=en&productNumber=227056> (accessed: March, 2020).
- [29] MSDS – M81802, <https://www.sigmaaldrich.com/MSDS/MSDS/DisplayMSDSPage.do?country=GB&language=en&productNumber=M81802> (accessed: March, 2020).
- [30] Candidate List of substances of very high concern for Authorisation – ECHA, <https://echa.europa.eu/candidate-list-table> (accessed: March, 2020).
- [31] A. E. Williams, P. J. Holliman, M. J. Carnie, M. L. Davies, D. A. Worsley, T. M. Watson, *J. Mater. Chem. A* **2014**, 2, 19338.

- [32] R. B. Palmer, *Toxicol. Rev.* **2004**, *23*, 21.
- [33] MSDS – B103608, <https://www.sigmaaldrich.com/MSDS/MSDS/DisplayMSDSPage.do?country=GB&language=en&productNumber=B103608> (accessed: March, 2020).
- [34] K. Knudsen, J. Greter, M. Verdicchio, *Clin. Toxicol.* **2008**, *46*, 187.
- [35] A. Osatiashtiani, A. F. Lee, K. Wilson, *J. Chem. Technol. Biotechnol.* **2017**, *92*, 1125.
- [36] I. T. Horváth, H. Mehdi, V. Fábos, L. Boda, L. T. Mika, *Green Chem.* **2008**, *10*, 238.
- [37] S. G. Wettstein, D. M. Alonso, Y. Chong, J. A. Dumesic, *Energy Environ. Sci.* **2012**, *5*, 8199.
- [38] I. Burgués-Ceballos, A. Savva, E. Georgiou, K. Kapnisis, P. Papagiorgis, A. Mousikou, G. Itskos, A. Othonos, S. A. Choulis, *AIP Adv.* **2017**, *7*, 115304.
- [39] M. Xu, W. Ji, Y. Sheng, Y. Wu, H. Cheng, J. Meng, Z. Yan, J. Xu, A. Mei, Y. Hu, Y. Rong, H. Han, *J. Nano. Eng.* **2020**, *74*, 104842.
- [40] J. C. Hamill, J. Schwartz, Y.-L. Loo, *Adv. Funct. Mater.* **2018**, *3*, 55.
- [41] J. Kim, B. W. Park, J. Baek, J. S. Yun, H. W. Kwon, J. Seidel, H. Min, S. Coelho, S. Lim, S. Huang, K. Gaus, M. A. Green, T. J. Shin, A. W. Y. Ho-Baillie, M. G. Kim, S. Il Seok, *J. Am. Chem. Soc.* **2020**, *142*, 6251.
- [42] K. Yan, M. Long, T. Zhang, Z. Wei, H. Chen, S. Yang, J. Xu, *J. Am. Chem. Soc.* **2015**, *137*, 4460.
- [43] Y. Ming, M. Xu, S. Liu, D. Li, Q. Wang, X. Hou, Y. Hu, Y. Rong, H. Han, *J. Power Sources* **2019**, *424*, 261.
- [44] K. P. Goetz, A. D. Taylor, F. Paulus, Y. Vaynzof, *Adv. Funct. Mater.* **2020**, *30*, 1910004.
- [45] W. Nie, H. Tsai, R. Asadpour, J. C. Blancon, A. J. Neukirch, G. Gupta, J. J. Crochet, M. Chhowalla, S. Tretiak, M. A. Alam, H. L. Wang, A. D. Mohite, *Science* **2015**, *347*, 522.
- [46] E. V. Péan, C. S. De Castro, M. L. Davies, *Mater. Lett.* **2019**, *243*, 191.
- [47] R. Kerremans, O. J. Sandberg, S. Meroni, T. Watson, A. Armin, P. Meredith, *Sol. RRL* **2019**, *4*, 1900221.
- [48] A. Pockett, D. Raptis, S. M. P. Meroni, J. Baker, T. Watson, M. Carnie, *J. Phys. Chem. C* **2019**, *123*, 11414.
- [49] Q. Wang, W. Zhang, Z. Zhang, S. Liu, J. Wu, Y. Guan, A. Mei, Y. Rong, Y. Hu, H. Han, *Adv. Energy Mater.* **2020**, *10*, 1.
- [50] I. Zimmermann, P. Gratia, D. Martineau, G. Grancini, J.-N. Audinot, T. Wirtz, M. K. Nazeeruddin, *J. Mater. Chem. A* **2019**, *7*, 8073.